NANO LETTERS

Letter

pubs.acs.org/NanoLett

Ultrasensitive Flow Sensing of a Single Cell Using Graphene-Based Optical Sensors

Fei Xing,[†] Gui-Xian Meng,[†] Qian Zhang,[‡] Lei-Ting Pan,[†] Peng Wang,[†] Zhi-Bo Liu,*[,†] Wen-Shuai Jiang,[†] Yongsheng Chen,[‡] and Jian-Guo Tian*[,†]

[†]The Key Laboratory of Weak Light Nonlinear Photonics, Ministry of Education, Teda Applied Physics School and School of Physics, Nankai University, Tianjin 300457, China

[‡]The Key Laboratory of Functional Polymer Materials and Center for Nanoscale Science and Technology, Institute of Polymer Chemistry, College of Chemistry, Nankai University, Tianjin 300071, China

Supporting Information

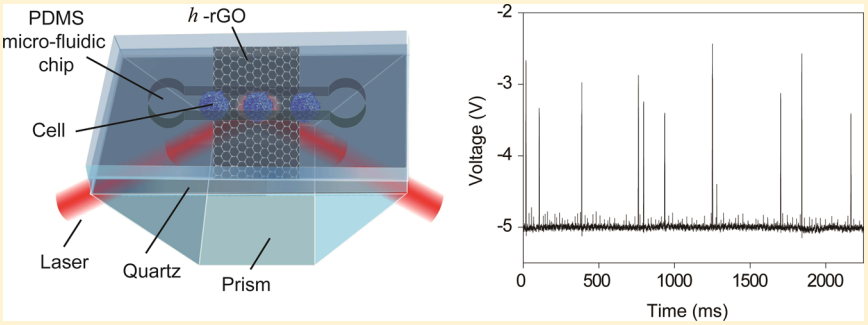

ABSTRACT: On the basis of the polarization-dependent absorption of graphene under total internal reflection, we designed a graphene-based optical refractive index sensor with high resolution of 1.7×10^{-8} and sensitivity of 4.3×10^{7} mV/RIU, as well as an extensive dynamic range. This highly sensitive graphene optical sensor enables label-free, live-cell, and highly accurate detection of a small quantity of cancer cells among normal cells at the single-cell level and the simultaneous detection and distinction of two cell lines without separation. It provides an accurate statistical distribution of normal and cancer cells with fewer cells. This facile and highly sensitive sensing refractive index may expand the practical applications of the biosensor.

KEYWORDS: *Single cell, graphene, optical sensor, cancer, polarization-dependent absorption*

An individual diseased cell frequently carries information that distinguishes it from normal cells. The accurate probing of diseased cells, particularly cancer cells, is critical prior to progression of the disease.[1,2] Microfluidic flow cytometry exhibits distinct advantages for detection at the single-cell level, including dynamic cell manipulation, isolation, sorting, small sample volumes, and repetitive usage without surface contamination.[3] Various methods have been developed for optical flow sensing of a single cell. At present, flow cytometers (FCMs)[4,5] and optofluidic circuits[6,7] are extensively employed due to their ability to provide label-free, real-time flow sensing of a single cell. However, these techniques require high-power lasers and do not accurately detect a complete signal for a single cell.

In recent years, graphene has emerged as a novel two-dimensional (2D) material in the field of material science due to its prominent intrinsic electronic, thermal, mechanical, structural, and chemical properties.[8−10] The electrical properties of graphene are sensitive to changes in the charge environment, which are induced by the reaction or adsorption of analytes on its surface. Sensitive flow sensing of a single cell based on graphene field-effect transistors has been developed.[11] However, transistor-based graphene flow sensing of a single cell requires changes in the current on the graphene surface to be measured. Therefore, the temporal and spatial resolutions are greatly restricted relative to the temporal and spatial resolutions of optical sensing. In addition, electrical measurement may cause damage to living cells, which may affect the accuracy of the detection results.[12] A highly sensitive graphene-based optical sensor is extremely useful as the flow detection platform of a single cell.

Currently, there are two optical methods to get a higher sensitivity and resolution in terms of the refractive index (RI) sensing. One method is based on sensitive surface plasmon resonance (SPR),[13−15] it is reported that the highest sensitivity and resolution are 5.7×10^{4} nm/RIU and 2.5×10^{-8}.[15] Another method is based on fibers,[16−18] and it is reported that the highest sensitivity and resolution are 3.0×10^{4} nm/RIU and 4.6×10^{-7}.[18] For graphene-based optical sensor, a resolution of 1×10^{4} for RI sensing has been obtain under total internal

Received: April 1, 2014
Revised: April 28, 2014
Published: May 5, 2014

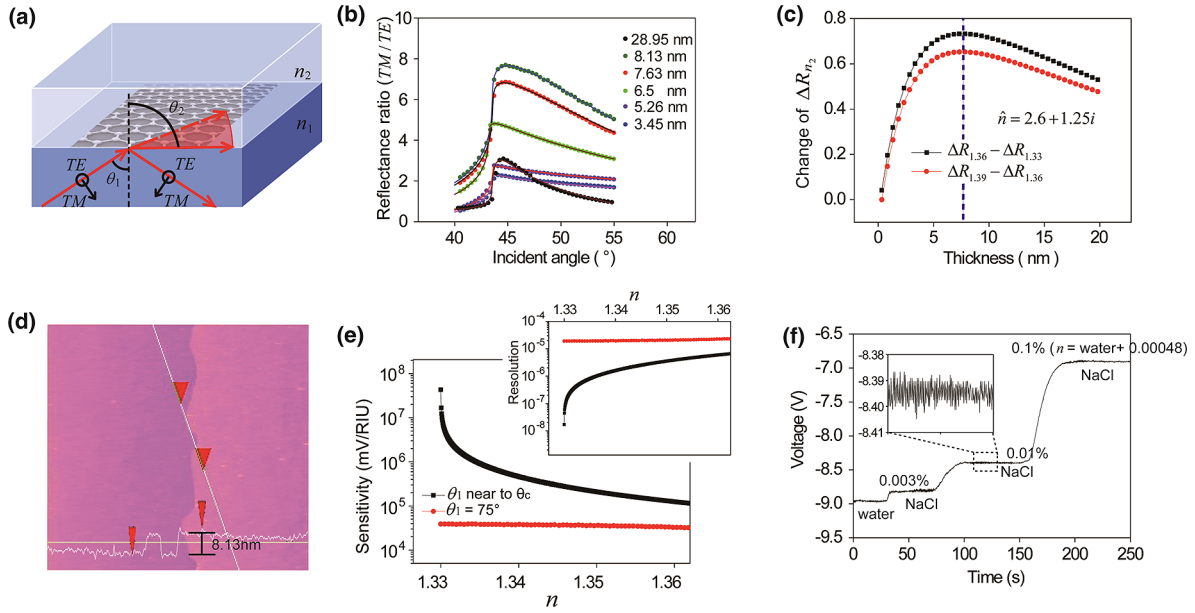

Figure 1. Schematic and results of the enhanced sensitivity and resolution of RI sensing. (a) Schematic of the enhanced sensitivity and resolution of RI sensing of *h*-rGO. (b) Angle-dependent reflectance ratio (TM/TE) plots of different thicknesses of *h*-rGO. (c) Calculating plots used to obtain the optimal thickness of *h*-rGO for maximum-enhancing resolution and sensitivity of RI sensing. (d) AFM image of the 8.13 nm thick *h*-rGO. (e) The black lines represent the RI-dependent sensitivity and resolution of the *h*-rGO-enhanced RI sensing with an 8.1 nm thick *h*-rGO. The red lines represent the RI-dependent sensitivity and resolution of RI sensing without enhancement. (f) Real-time signal of different ultralow concentrations of NaCl solution.

reflection (TIR) structure.[19] The strong broadband absorption of graphene causes it to exhibit different reflectance for transverse electric (TE) and transverse magnetic (TM) modes under TIR, which is sensitive to the media RI that is in contact with the graphene.[19−21] The enhanced sensitivity of RI sensing for the flow sensing of a weak signal remains a considerable challenge.

In this work, we obtain an ultrasensitive graphene optical sensor by controlling the thickness of high-temperature reduced graphene oxide (*h*-rGO). The limits of sensitivity and resolution for RI sensing are increased to 4.3×10^7 mV/RIU and 1.7×10^{-8}, respectively. The resolution is the highest values reported for RI sensors. With its ultrahigh sensitivity, this graphene optical sensor produces an extensive dynamic range through adjustment of the incidence angle and incident power. The optimal thickness of *h*-rGO is approximately 8 nm, as determined by theoretical simulation and experimental validation. In the experiment, the minor difference between the RI of 0.003% sodium chloride solution ($n = n_{water} + 0.000144$) and the RI of water can be distinguished with a high signal-to-noise ratio (SNR). Using this method, we demonstrated the ultrasensitive and extensive dynamic range sensing of a single Jurkat cell on the graphene optical sensor platform, which exhibits ultrahigh sensitivity and resolution for the media RI at a certain depth range from the graphene surface. We achieved a one-time detection of normal lymphocytes with a small number of Jurkat cells at the single-cell level. The Jurkat cell is a type of lymphocyte cancer cell. We demonstrated that the graphene-based optical single-cell sensor (GSOCS) exhibits high sensitivity to a single cell. To verify the sensitivity and applicability of this sensor, standard polystyrene (PS) microspheres were probed as they rolled across a detection window. The experimental results concur with the results of the theoretical simulation. A complete voltage signal of a single PS microsphere can be accurately obtained. The GSOCS provides an accurate statistical distribution of different sizes of PS microspheres, lymphocytes, and Jurkat cells for an extensive dynamic range.

The improved model of RI sensing is presented in Figure 1a. The model used in this investigation consists of a graphene layer inserted between a high-index medium (medium 1, refractive index n_1) and a low-index medium (medium 2, refractive index n_2) (see Supporting Information for details). The difference between the reflectance of the TM mode and the reflectance of the TE mode is the sensitivity to variations in the refractive index n_2 under the fixed conditions n_1.[19] The resolution and sensitivity of detection can be increased with a fixed thickness of graphene when the incident angle θ_1 is near the critical angle θ_c. With a fixed θ_1, the incident light cannot be completely reflected as the refractive index n_2 increases. The resolution and sensitivity of the RI measurement can be significantly enhanced by controlling the thickness of graphene.

Figure 1b displays plots of angle-dependent reflectance ratios for different *h*-rGO thicknesses. The solid lines represent the calculated results and the real points represent the experimental results. The parameters of the different thicknesses of *h*-rGO are provided in Supporting Information Table S1. The best-fitting optical constant $\hat{n}$ of *h*-rGO is obtained with $\hat{n} = 2.6 + 1.25i$. Therefore, the optical constant $\hat{n} = 2.6 + 1.25i$ of *h*-rGO is used to calculate the optimal thickness of *h*-rGO for a maximum enhanced resolution and sensitivity of RI sensing. Figure 1c shows how to determine the optimum thickness of *h*-rGO, where $\Delta R_{n_2} = R_{TE} - R_{TM}$ is the reflectance difference for TE and TM polarized light when the refractive index of medium 2 is n_2. The two lines are plots of changes of ΔR_{n_2} ($\Delta R_{1.36} - \Delta R_{1.33}$ and $\Delta R_{1.39} - \Delta R_{1.36}$) when the n_2 changes from 1.36 to 1.33 and 1.39 to 1.36. The corresponding incident angle is chosen to be 65.7° and 67.6° (see Supporting Information for details). The incident light of the TE or TM

dx.doi.org/10.1021/nl5012036 | *Nano Lett.* 2014, 14, 3563−3569

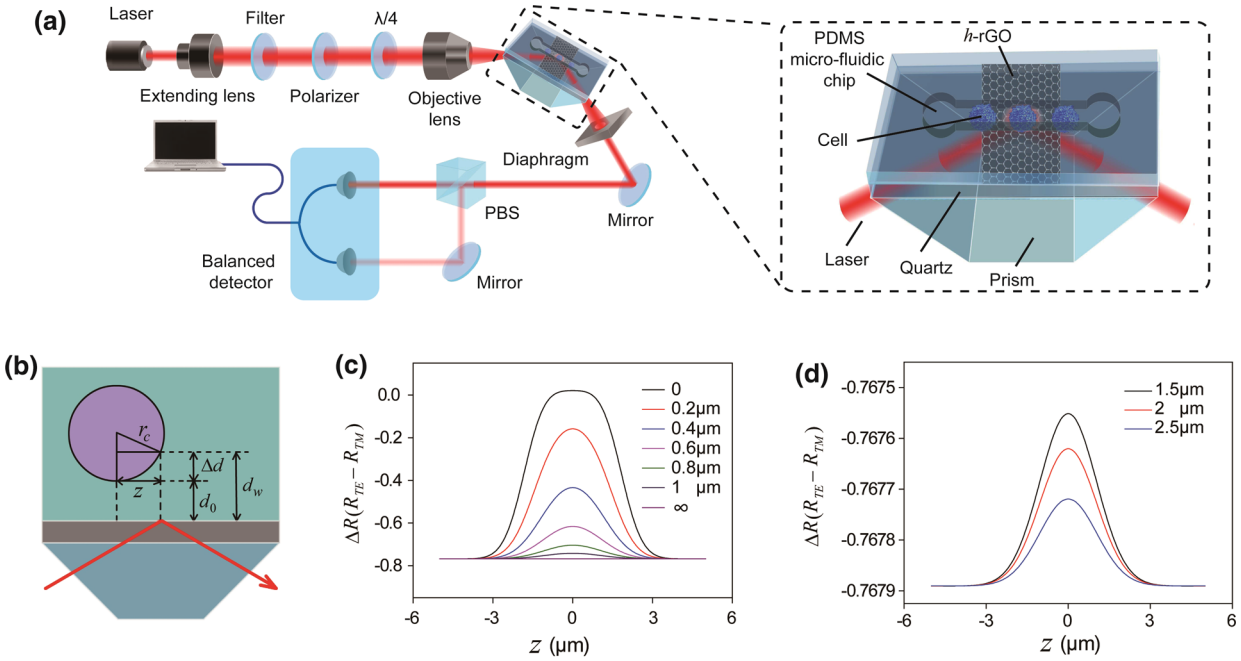

Figure 2. Experimental setup and theoretical simulation. (a) Flow-sensing system for a single-cell setup. The inset provides the schematic of the GSOCS, which is a PDMS microfluidic chip/*h*-rGO/quartz sandwich structure on the prism. (b) Theoretical model of the flow sensing of a single cell. (c,d) Theoretical simulation results for a single PS microsphere that rolls across the detection window of the GSOCS with increasing d_0.

mode is 80 μW, n_{quartz} = 1.47, and n_{water} = 1.33. The black line plot illustrates that the greatest signal change is approximately 0.75, which corresponds to an 8 nm thick *h*-rGO. The red line in Figure 1c illustrates that large signal changes in ΔR can be adjusted to any RI range by adjusting the incidence angle θ_1 (Supporting Information Figure S1). Figure 1d displays an atomic force microscopy (AFM) image of an 8.13 nm thick *h*-rGO. The thickness of the *h*-rGO can be accurately controlled within the range of a few nanometers by varying the concentrations of graphene oxide (GO) and the speeds of the spin coating (Supporting Information Figures S2 and S3).

In order to achieve the most sensitive sensing, ~8 nm thick *h*-rGO is the optimal choice as a sensing layer compared with other types of graphene.[22−24] Monolayer and few layers chemical vapor deposition (CVD) graphene exhibit distinct advantages, including low defects, uniform, and well-defined structure. It should be the optimal choice as a sensing layer. However, in order to achieve the most sensitive sensing, it can be concluded that the optimal thickness of graphene is ~20 layers (Supporting Information Figure S4) with the standard optical constants of graphene ($\hat{n}$ = 2.6 + 1.3i)[25−27] by calculation. For ~20 layers graphene, it is difficult to grow by the CVD method. In addition, CVD graphene cannot be directly applied to the transparent medium, and it must go through the transfer process before being used. During the transfer process of graphene, the problems of damage, pollution, and folds are inevitable. Meanwhile, the graphene sensing layer needs to be applied in the microfluidic channel. The transfer process of CVD graphene brought a large surface roughness (Supporting Information Figure S5), easy to fall off (Supporting Information Figure S6), and decline in polarization-dependent absorption effect (Supporting Information Figure S7). Therefore, CVD graphene is unsuitable as the sensing layer for high sensitive sensing of refractive index based on the polarization-dependent absorption effect of graphene, and rGO is a better candidate.

The resolution and sensitivity, which are the important parameters of RI sensing, are calculated with the following formula

$$S = \frac{\left.\frac{d\Delta R}{dn}\right|_{n=n_2} \cdot P_0}{\alpha} \quad (1)$$

$$L = \frac{V_n}{S} \quad (2)$$

where S is the sensitivity of RI sensing, L is the resolution of RI sensing, P_0 is the incident power of the TE or TM mode, α is the response of the balanced detector, and V_n is the noise value. The power was fixed to 80 μW, and the incidence angle was close to the critical incidence. The thickness of the *h*-rGO is 8.1 nm, and its optical constant is $\hat{n}$ = 2.6 + 1.25i; α is 0.00361 μW/mV, and V_n is approximately 10 mV. Figure 1e presents the RI-dependent resolution and sensitivity of the *h*-rGO-enhanced RI sensor under these conditions. The limits of resolution and sensitivity of the *h*-rGO-enhanced RI sensing are 1.7×10^{-8} and 4.3×10^{7} mV/RIU, respectively, when $P_0 = P_{TE} = P_{TM}$ = 80 μW. This resolution is the highest reported for RI sensing.[13−18] Different ultralow concentrations of sodium chloride solution were detected in real time by an *h*-rGO-enhanced RI sensor, as shown in Figure 1f. The minor and distinct differences between the RI of 0.003% sodium chloride solution ($n = n_{water}$ + 0.000144) and the RI of water are approximately 210 mV. The inset presents an enlarged V_n of approximately 10 mV.

Figure 2a is the experimental setup of the flow sensing system for a single cell. Light from a He−Ne laser at 632.8 nm is adjusted to circularly polarized light by a polarizer and quarter-wave plate. The circularly polarized light is focused on the GSOCS at the center of its microfluidic channel. The inset of Figure 2a provides the schematic of the GSOCS, which consists of a polydimethylsiloxane (PDMS) microfluidic chip/

dx.doi.org/10.1021/nl5012036 | Nano Lett. 2014, 14, 3563−3569

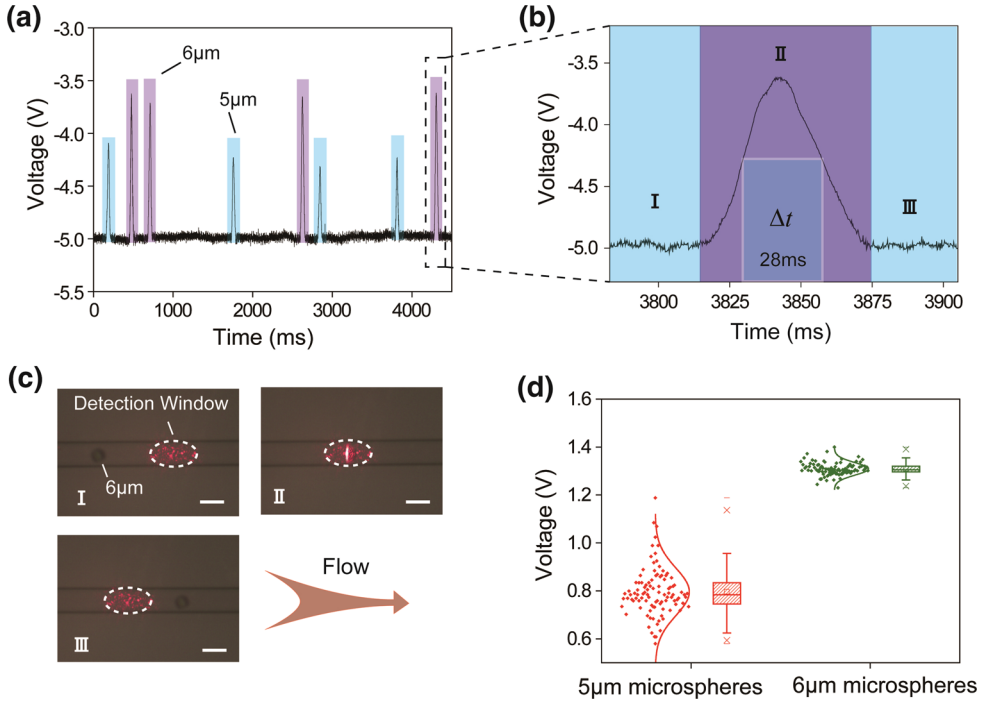

Figure 3. Experimental results of the GSOCS by detecting the PS microspheres. (a) Discrete time-dependent changes in voltage that correspond to PS microspheres as they roll across the *h*-rGO detection window. The light blue and light purple areas represent the discrete voltage signals of 5 and 6 μm PS microspheres, respectively. (b) Entire sensing process for a single PS microsphere detected by the GSOCS in which Δt represents the time changes for a PS microsphere that rolls across the *h*-rGO detection window. (c) Microscopic images of the *h*-rGO detection window as a 6 μm PS microsphere rolls across it. The scale bar is 10 μm, the flow rate is 3 μL/h, and the height of microfluidic channel is approximately 6.5 μm. (d) Boxplot of the voltage signals for PS microspheres.

h-rGO/quartz sandwich structure on the prism. The diaphragm is used to further refine the detection range of the focused light spot, which can be controlled at a minimum of approximately 1 μm by probing. After being separated into TE and TM modes by a polarization beam splitter (PBS), the reflected light is detected by a balanced detector. The initial voltage signal of the balanced detector is not in an equilibrium state due to the absorption differences between the TE and TM modes for *h*-rGO.

The theoretical model of the flow sensing of a single cell is constructed on the prism *h*-rGO film/water/cell four-layer structure by transfer matrix theory (Figure 2b) (see Supporting Information for details). The cell is considered to be a semi-infinite medium with a specific RI (n_c = 1.36) and a circle in the lower half. The cell flow processes were considered to represent the changes in thickness of the water layer, and the light spot is sufficiently small (Figure 2b). The relationship between the thickness of the water layer (d_w) and the distance from the center of the cell (z) was $d_w = d_0 + \Delta d = d_0 + r_c - (r_c^2 - z^2)^{1/2}$ ($-r_c \leq z \leq r_c$), where d_0 is the vertical distance from the lowest point of cell to the *h*-rGO film and r_c is the cell radius. When d_0 is zero, we consider that the cell flows close to the *h*-rGO film. Because the refractive index of the flowing liquid is relatively stable, the refractive index of the flowing cells and microspheres exists some uncertainty. In order to achieve the desired results, the incident power was increased to $P_0 = P_{TE} = P_{TM}$ = 160 μW in the process of theoretically simulated and used to detect PS microspheres. For a fixed θ_1 of 67.6° the minimum signal change for ΔR that can be detected in the experiment is approximately 0.015%. The simulation results illustrate that an ultrahigh resolution capability can be obtained for the flow sensing of a single cell when $d_0 \leq 1$ μm (Figure 2c). The signal changes of ΔR weaken rapidly with increasing d_0. Figure 2d illustrates that when d_0 = 2.5 μm, the signal change of ΔR is reduced to approximately 0.017%, which is near the detection limit of the GSOCS. Therefore, the detection range of $d_0 \leq 2.5$ μm is employed in the experiment. The sensing signals with ultrahigh sensitivity can be detected from any point within the entire range of regional detection. The results are credible even for sensing signals in which $d_0 \leq 2.5$ μm.

We verified that the GSOCS had ultrahigh sensitivity to a single cell or particle by detecting standard PS microsphere samples. The fixed incidence angle θ_1 is 67.6°, the incident power $P_0 = P_{TE} = P_{TM}$ = 160 μW, and the diameters of the PS microspheres detected in the experiment are 5 and 6 μm. Figure 3a presents the time-dependent changes in voltage that correspond to mixed 5 and 6 μm PS microspheres as they roll across the detection window. In the one-time detection plot, the light blue and light purple areas represent the discrete voltage signals of 5 and 6 μm microspheres, respectively. The counting and distinction capabilities of single 5 and 6 μm PS microspheres are distinctly presented with significant differentiation as they roll across the detection window without separation. The advantages of the GSOCS, which include real-time detection and rapid response, are also reflected in Figure 3a. At a high flow rate of 3 μL/hour,[11] the baseline voltage signals remain relatively constant at -5 ± 0.01 V. This result demonstrates the good sensing repeatability of the *h*-rGO sensor platform without surface contamination. Figure 3b presents the entire sensing process for a single PS microsphere detected by the GSOCS; the result corresponds with the simulation results in Figure 2c. The change in voltage signals caused by the variation in uniformity of the microsphere surface and the flow factors of the microfluid are detectable even in

dx.doi.org/10.1021/nl5012036 | *Nano Lett.* 2014, 14, 3563−3569

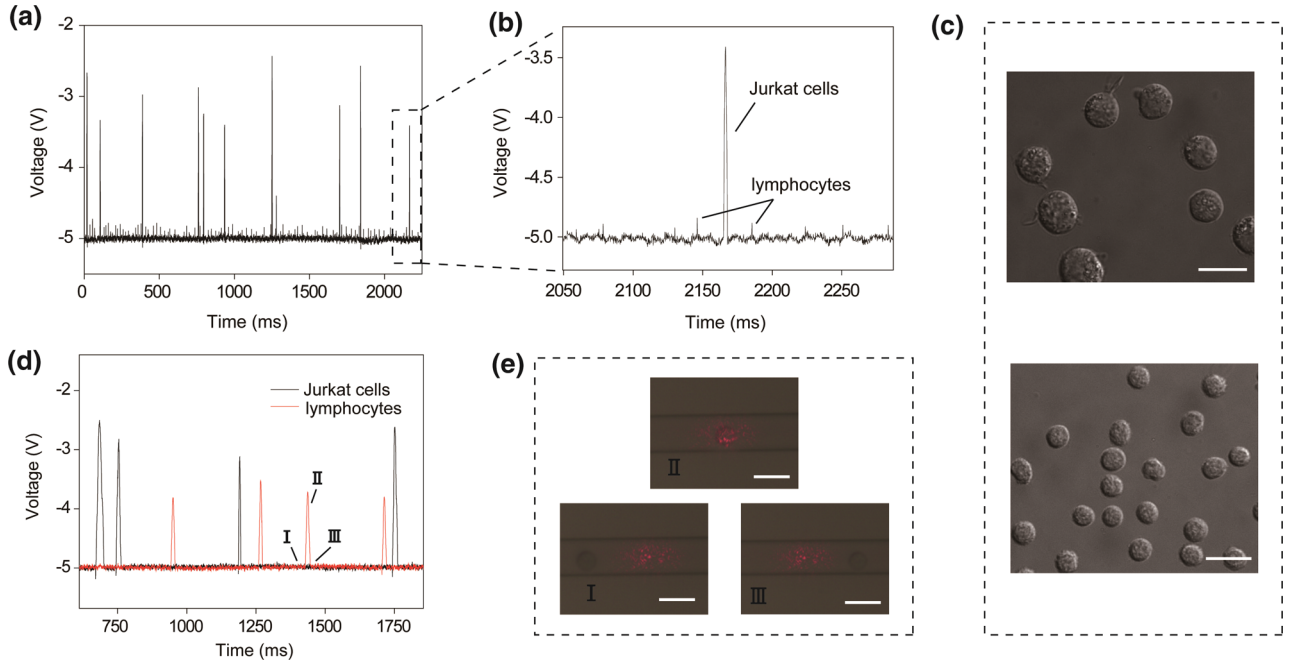

Figure 4. Results of single cell detection by the GSCOS in a microfluidic channel and its microscopic characterization. (a) Discrete time-dependent changes in voltage that correspond to mixed lymphocytes and Jurkat cells as they roll across the *h*-rGO detection window. (b) Enlarged images of panel a for certain positions in which the voltage signals are clearly depicted. The high and low signals represent Jurkat cells and lymphocytes, respectively, as they roll across the detection window. (c) Microscopic images of Jurkat cells (top) and lymphocytes (bottom); the scale bar is 15 μm. (d) Discrete time-dependent changes in voltage that correspond to a single lymphocyte or Jurkat cell as it rolls across the detection window. The black and red lines represent Jurkat cells and lymphocytes, respectively. (e) Microscopic images of the *h*-rGO detection window as lymphocytes roll across it. The scale bar is 15 μm, and the height of microfluidic channel is approximately 9 μm.

different locations of a single microsphere. The SNR of a single PS microsphere plot is approximately 150. The regions I–II–III in Figure 3b correspond to the regions I–II–III in Figure 3c in which the flow direction is oriented from left to right. The full width at half-maximum (fwhm) of the plot is used to determine the time changes (Δt) for the PS microsphere that rolls across the detection window, which reflects the relative size and flow rate of a single PS microsphere. In the plot, the Δt for the single PS microsphere is approximately 28 ms. The fwhm statistical results of 6 μm PS microspheres detected by the GSOCS is shown in Supporting Information Figure S8. We demonstrate that voltage signals can respond rapidly and accurately in tens of milliseconds. Figure 3d presents a boxplot of voltage signals for 5 and 6 μm PS microspheres. The 5 and 6 μm PS microspheres roll across the same microchannel and induce voltage changes of 0.797 ± 0.099 V and 1.309 ± 0.003 V, respectively; the statistical number is 100, and the height and width of the microchannel is approximately 6.5 and 10 μm. The different levels of voltage rise measured by the GSOCS illustrates the ability to differentiate between the 5 and 6 μm PS microspheres.

Cancer detection is a continuous global problem. The accurate probing of cancer cells on a single-cell level prior to the progression of cancer is critical. To satisfy their demand to divide indefinitely, cancer cells are generally larger than normal cells.[28,29] The RIs of cancer cells are also significantly larger than those of normal cells. In this study, lymphocytes and Jurkat cells extracted from the blood are detected by the GSOCS in a microfluidic channel. To prevent cancer, we mixed a low percentage (1%) of Jurkat cells with normal lymphocytes and detected the signal changes in voltage with the GSOCS. Figure 4a presents the discrete time-dependent changes in voltage that correspond to the mixed lymphocytes and Jurkat cells as they roll across the *h*-rGO detection window. The height and width of the microfluidic channel are approximately 12.5 and 20 μm. A high flow rate of approximately 7 μL/h is used to make the cells roll across the microfluidic channels smoothly and rapidly.[11] The variation in peak voltage illustrates the sensor's ability to differentiate the two cell lines on a single-cell level. In addition, the voltage signal for each cell is exhibited by a sharp line, which represents the high sensitivity and resolution of the GSOCS to cell signal detection. Detailed information is provided in Figure 4b. The high voltage level represents the signal from the Jurkat cell, and the low voltage level represents the signal from the lymphocyte. Although the voltage signal of the lymphocyte is small, it is sufficiently credible. This result is precisely confirmed by the extensive dynamic range of the GSOCS. Figure 4c presents the microscopic images of Jurkat cells (top) and lymphocytes (bottom). The average size of the Jurkat cells is greater than the average size of the lymphocytes, which is converted to an average refractive index that is accurately detected by the GSOCS. The Jurkat cells and lymphocytes are detected by the GSOCS for different heights of microfluidic channels that correspond to their size. The heights of the microfluidic channel for lymphocytes and Jurkat cells are approximately 9 and 12.5 μm, and the width of the microfluidic channel for lymphocytes and Jurkat cells are approximately 15 and 20 μm, respectively. Figure 4d presents the discrete time-dependent changes in voltage that correspond to a single lymphocyte or Jurkat cell as it rolls across the detection window. Regions I–II–III in Figure 4d correspond to regions I–II–III in Figure 4e, in which the flow direction is oriented from left to right. The result reveals a distinct difference between the two types of cells

dx.doi.org/10.1021/nl5012036 | *Nano Lett.* 2014, 14, 3563–3569

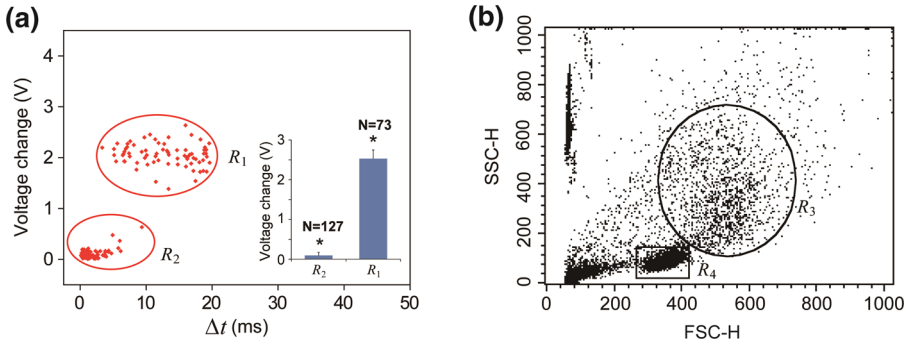

Figure 5. Statistical results of the detection of mixed cells. (a) Statistical plot of mixed cells of Jurkat cells and lymphocytes as detected by the GSOCS. Regions R_1 and R_2 represent the statistical distribution of Jurkat cells and lymphocytes, respectively. The statistical number is 200. The inset is the histograms with the number of counts for each cell population and the data shown represents the mean ± SD, where SD is standard deviation, * indicates statistical significance between each cell population ($P < 0.01$), and N is the number of each cell population. (b) Statistical plot of mixed cells of Jurkat cells and lymphocytes, as detected by commercial FCM. Regions R_3 and R_4 represent the statistical distribution of Jurkat cells and lymphocytes, respectively; the statistical number is 10 000. Statistical chart of mixed cells as detected by the commercial FCM.

in the microchannels that correspond with their size. Differences in the same types of cells are evident due to the differences in size and endoplasmic matter.[28,29]

The study of the classified statistics of cells is an important aspect of biology and medicine.[30] Although such research does not provide comprehensive information regarding individual cells, it serves as an important reference for statistical proportion and distribution, especially regarding disease diagnosis. Figure 5a presents the classified statistics for Jurkat cells and lymphocytes detected by the GSOCS in the same microchannel. The Jurkat cell produces a voltage change of 2.053 ± 0.22 V and induces a time change of 25.843 ± 4.273 ms. Also, the inset in Figure 5a is the corresponding histograms. The voltage changes for lymphocytes occurs within a narrow range near zero with a concentrated distribution. The regions R_1 and R_2 represent the Jurkat cells and lymphocytes, respectively. The mixing ratio of the Jurkat cells to the lymphocytes is 1:1 and the statistical number is 200. Figure 5b provides the statistical chart for the same cell samples detected by the commercial FCM, and the regions R_3 and R_4 represent the Jurkat cells and lymphocytes, respectively. Their statistical number is 10 000. A comparison with the statistical results of the commercial FCM indicates that the statistical results of the GSOCS also demonstrate the sensor's ability to distinguish between cell lines. In addition, accurate statistics are obtained with a small number of cells.

In the same type of sensor, FCM and optofluidic circuit are extensively employed due to their ability to provide label-free, real-time flow sensing of cells. For the label-free FCM, it was only able to make statistics on the cell type by a large number of cells and capture a point for each cell. Meanwhile, it needed to count a large numbers of cells. For the optofluidic circuit, it was able to obtain complete information on the cell, but the detection method of transmission and scattering signals is difficult to meet the need of high sensitivity measurement. Also, both of the two methods need a high cost and are unable to distinguish low proportion cells at different cell types. However, the GSOCS is capable of accurately detecting a small amount of diseased cells, such as cancer cells, among a large number of normal cells. Even cancer cells with extremely low proportions can be detected due to the precise sensing capabilities of a single cell. The GSOCS can provide comprehensive information regarding each cell signal, which is extremely important for research on the cell submicroscopic structure.

In summary, we designed a graphene-based optical refractive index sensor with the high sensitivity of 4.3×10^7 mV/RIU and resolution of 1.7×10^{-8}, as well as large dynamic range. The ultrahigh sensitivity and resolution of the GSOCS regarding the RI play a significant role in the promotion of dynamic research on a single cell in the submicroscopic structure of a cell. In addition, the sensor's ultrahigh resolution and sensitivity to RI measurements can be extended to other areas, such as drug discovery, environmental monitoring, and gas- and liquid-phase chemical sensing.

■ ASSOCIATED CONTENT

Supporting Information

Materials and methods, supplementary Figures S1–S11, and Table S1. This material is available free of charge via the Internet at http://pubs.acs.org.

■ AUTHOR INFORMATION

Corresponding Authors

*E-mail: rainingstar@nankai.edu.cn.
*E-mail: jjtian@nankai.edu.cn.

Notes

The authors declare no competing financial interest.

■ ACKNOWLEDGMENTS

The authors thank The Chinese National Key Basic Research Special Fund (Grant 2011CB922003), The Natural Science Foundation of China (Grants 11174159, 11374164, and 11204142), and the Natural Science Foundation of Tianjin (Grant 13JCYBJC16300).

■ REFERENCES

(1) Backman, V.; Wallace, M. B.; Perelman, L. T.; Arendt, J. T.; Gurjar, R.; Müller, M. G.; Zhang, Q.; Zonios, G.; Kline, E.; McGillican, T.; Shapshay, S.; Valdez, T.; Badizadegan, K.; Crawford, J. M.; Fitzmaurice, M.; Kabani, S.; Levin, H. S.; Seiler, M.; Dasari, R. R.; Itzkan, I.; Van Dam, J.; Feld, M. S. *Nature* **2000**, *406*, 35–36.

(2) Hingorani, S. R.; Petricoin, E. F., III; Maitra, A.; Rajapakse, V.; King, C.; Jacobetz, M. A.; Ross, S.; Conrads, T. P.; Veenstra, T. D.; Hitt, B. A.; Kawaguchi, Y.; Johann, D.; Liotta, L. A.; Crawford, H. C.; Putt, M. E.; Jacks, T.; Wright, C. V. E.; Hruban, R. H.; Lowy, A. M.; Tuveson, D. A. *Cancer Cell* **2003**, *4*, 437–450.

(3) Bhagat, A. A. S.; Bow, H.; Hou, H. W.; Tan, S. J.; Han, J.; Lim, C. T. *Med. Biol. Eng. Comput.* **2010**, *48*, 999–1014.

(4) Davey, H. M.; Kell, D. B. *Microbiol. Mol. Biol. Rev.* **1996**, *60*, 641−696.
(5) Gawad, S.; Schildb, L.; Renauda, P. *Lab Chip* **2001**, *1*, 76−82.
(6) Kim, M.; Hwang, D. J.; Jeon, H.; Hiromatsu, K.; Grigoropoulos, C. P. *Lab Chip* **2009**, *9*, 311−318.
(7) Liang, X. J.; Liu, A. Q.; Lim, C. S.; Ayi, T. C. *Sens. Actuators A* **2007**, *133*, 349−354.
(8) Weiss, N. O.; Zhou, H.; Liao, L.; Liu, Y.; Jiang, S.; Huang, Y.; Duan, X. *Adv. Mater.* **2012**, *24*, 5782−5825.
(9) Zhu, Y.; Murali, S.; Cai, W.; Li, X.; Suk, J. W.; Potts, J. R.; Ruoff, R. S. *Adv. Mater.* **2010**, *22*, 3906−3924.
(10) Wei, D.; Liu, Y. *Adv. Mater.* **2010**, *22*, 3225−3241.
(11) Ang, P. K.; Li, A.; Jaiswal, M.; Wang, Y.; Hou, H. W.; Thong, J. T. L.; Lim, C. T.; Loh, K. P. *Nano Lett.* **2011**, *11*, 5240−5246.
(12) Silve, A.; Leray, I.; Mir, L. M. *Bioelectrochemistry* **2012**, *87*, 260−264.
(13) Giorgini, A.; Avino, S.; Malara, P.; Gagliardi, G.; Casalino, M.; Coppola, G.; Iodice, M.; Adam, P.; Chadt, K.; Homola, J.; Natale, P. D. *Opt. Lett.* **2013**, *38*, 1951−1953.
(14) Wu, L.; Chu, H. S.; Koh, W. S.; Li, E. P. *Opt. Express* **2010**, *18*, 14395−14400.
(15) Slavík, R.; Homola, J. *Sens. Actuators, B* **2007**, *123*, 10−12.
(16) Mileńko, K.; Hu, D. J. J.; Shum, P. P.; Zhang, T.; Lim, J. L.; Wang, Y.; Woliński, T. R.; Wei, H.; Tong, W. *Opt. Lett.* **2012**, *37*, 1373−1375.
(17) Frosz, M. H.; Stefani, A.; Bang, O. *Opt. Express* **2011**, *19*, 10471−10484.
(18) Wu, D. K. C.; Kuhlmey, B. T.; Eggleton, B. J. *Opt. Lett.* **2009**, *34*, 322−324.
(19) Xing, F.; Liu, Z.; Deng, Z.; Kong, X.; Yan, X.; Chen, X.; Ye, Q.; Zhang, C.; Chen, Y.; Tian, J. *Sci. Rep.* **2012**, *2*, 908.
(20) Ye, Q.; Wang, J.; Liu, Z.; Deng, Z.; Kong, X.; Xing, F.; Chen, X.; Zhou, W.; Zhang, C.; Tian, J. *Appl. Phys. Lett.* **2013**, *102*, 021912.
(21) Xing, F.; Chen, X.; Liu, Z.; Zhang, Q.; Yan, X.; Chen, Y.; Tian, J. *Appl. Phys. Lett.* **2013**, *102*, 253501.
(22) Kurkina, T.; Sundaram, S.; Sundaram, R. S.; Re, F.; Masserini, M.; Kern, K.; Balasubramanian, K. *ACS Nano* **2012**, *6*, 5514−5520.
(23) Pei, S. F.; Cheng, H. M. *Carbon* **2012**, *50*, 3210−3228.
(24) Lee, S.; Jang, H. Y.; Jang, S.; Choi, E.; Hong, B. H.; Lee, J.; Park, S.; Ahn, J. *Nano Lett.* **2012**, *12*, 3472−3476.
(25) Blake, P.; Hill, E. W.; Neto, A. H. C.; Novoselov, K. S.; Jiang, D.; Yang, R.; Booth, T. J.; Geim, A. K. *Appl. Phys. Lett.* **2007**, *91*, 063124.
(26) Yu, V.; Hilke, M. *Appl. Phys. Lett.* **2009**, *95*, 151904.
(27) Wang, X.; Zhao, M.; Nolte, D. D. *Appl. Phys. Lett.* **2009**, *95*, 081102.
(28) Bourgaize, D.; Jewell, T. R.; Buiser, R. G. *Biotechnology: Demystifying the Concepts*; Addison Westley Longman: San Francisco, 1999.
(29) Sherr, C. J. *Science* **1996**, *274*, 1672−1677.
(30) Glaser, S. L.; Dorfman, R. F.; Clarke, C. A. *Cancer* **2001**, *92*, 218−224.